A high voltage solid state symmetric supercapacitor based on graphene–polyoxometalate hybrid electrodes with a hydroquinone doped hybrid gel- electrolyte†

Deepak P. Dubal,*[a] Jullieth Suarez-Guevara,[a] Dino Tonti,[b] Eduardo Enciso[c] and Pedro Gomez-Romero*[a]

[a]Catalan Institute of Nanoscience and Nanotechnology (ICN2), CSIC and The Barcelona Institute of Science and Technology, Campus UAB, Bellaterra, 08193 Barcelona, Spain. E-mail: dubaldeepak2@gmail.com; pedro.gomez@cin2.es; Fax: +34 5929951; Tel: +34 9373609/+34 5929950

[b]ICMAB (CSIC), Campus UAB, E-08193 Bellaterra, Barcelona, Spain

[c]Departamento de Química-Fisica I, Facultad de Ciencias Quimicas, Universidad Complutense de Madrid (UCM) Campus Moncloa, Madrid, Spain

*Pedro.gomez@icn2.cat

Abstract

In pursuit of high capacitance and high energy density storage devices, hybrid materials have quickly garnered well-deserved attention based on their power to merge complementary components and properties. Here, we report the fabrication of all-solid state symmetric supercapacitors (ASSSC) based on a double hybrid approach combining a hybrid electrode (reduced graphene oxide–phoshomolybdate, rGO–PMo_{12}) and a hybrid electrolyte (hydroquinone doped gel-electrolyte). To begin with, a high-performance hybrid electrode based on $H_3PMo_{12}O_{40}$ nanodots anchored onto rGO was prepared (rGO–PMo_{12}). Later, an all-solid state symmetric cell based on these rGO–PMo_{12} electrodes, and making use of a polymer gel-electrolyte was assembled. This symmetric cell showed a significant improvement in cell performance. Indeed, it allowed for an extended potential window by 0.3 V that led to an energy density of 1.07 mW h cm^{-3}. Finally, we combined these hybrid electrodes with a hybrid electrolyte incorporating an electroactive species. This is the first proof-of-design where a redox-active solid-state gel-electrolyte is applied to rGO–PMo_{12} hybrid supercapacitors to accomplish a significant enhancement in the capacitance. Strikingly, a further excellent increase in the device performance (energy density 1.7 mW h cm^{-3}) was realized with the hybrid electrode–hybrid electrolyte combination cell as compared to that of the conventional electrolyte cell. Thus, this unique symmetric device outclasses the high-voltage asymmetric counterparts under the same power and represents a noteworthy advance towards high energy density supercapacitors.

Introduction

Energy storage materials have been widely researched in order to meet the increasing demand for high energy, high power and cost-effective storage systems.[1–3] Thus, various electrochemical energy storage devices have been proposed with batteries and supercapacitors as complementary technologies.[2] Batteries take advantage of a bulk charge storage mechanism, hence exhibit a high energy density but they suffer from a low power and cycling stability. In great contrast, supercapacitors store charge through surface adsorption (non-faradaic) and surface redox reaction (pseudo-capacitor), hence possess high power density and excellent cycling stability, sacrificing energy storage ability.[4]

The emerging new concept of hybrid electrodes combines the high energy density characteristic of batteries with the high power and long-term stability of supercapacitors.[2] These hybrid electrodes can be made by the combination of non-faradaic materials (commonly, carbons) and faradaic materials (transition metal oxides, polyoxometalates, conducting polymers, etc.).[5–7] The challenge for fabrication of hybrid electrodes is to find suitable redox species (faradaic) to be anchored onto the carbon surface, thus effectively increasing the electrochemical activity of the electrodes and enhancing the performance of the device.

Polyoxometalates (POMs) are redox-active molecular clusters combining oxygen and early transition metals (*e.g.*, M = V, Nb, Ta, Mo, and W) at their highest oxidation states. POMs are molecular oxides which contain tens to hundreds of metal atoms that reach nuclearities as high as 368 metal atoms in one single cluster molecule.[8,9] They are well-suited to achieve a high capacity for energy storage applications due to their fast and reversible multi-electron redox reactions. On the other hand, due to the high solubility of these POMs in aqueous and polar organic solvents, their use as electrode materials requires their anchoring onto a variety of conducting substrates, from conducting polymers[10,11] to graphene,[12] carbon nanotubes (CNTs),[13,14] or activated carbons (AC).[15] This anchoring prevents the dissolution of POMs into the electrolyte and provides the necessary electrical conductivity. The smallest and simplest

POMs present the Keggin structure (corresponding to the general composition $[AM_{12}O_{40}]^{n-}$) and are electrochemically active and very stable in acidic aqueous electrolytes.

In addition to the anchoring of redox-active species for added energy storage, another approach for the fabrication of supercapacitors with high energy density is the widening of their operational voltage window (since, E = 0.5CV2). In this sense, construction of asymmetric supercapacitors with pseudocapacitive material cathodes and EDLC carbon anodes in aqueous electrolytes is the most frequently adopted strategy.[16]

However, energy density is still restricted by the carbon anodes and undermined by the large mass-loading needed to match the pseudocapacitive cathodes. On the other hand, constructing symmetric capacitors with two identical electrodes can effectively solve this problem; however, this requires strict criteria on the electrodes pairing to give a high operation voltage and high- level capacitance with good rate capability. Generally, designing high-rate electrodes with a tailor-made porosity and electronically conductive scaffold to allow facile electrolyte access and fast faradic response at high power remains a crucial challenge.

In this context, we carefully prepared three-dimensional (3D) reduced graphene oxide (rGO) with a hierarchical open-pore structure through a modified Hummers method. Subsequently, phosphomolybdic acid ($H_3PMo_{12}O_{40}$) (PMo_{12} in short) was homogeneously and efficiently anchored onto the surface of rGO nanosheets (Fig. 1). In order to demonstrate the electro- chemical performance of this hybrid material, we fabricated symmetrical supercapacitors with rGO–PMo_{12} electrodes and H_2SO_4/PVA gel electrolytes. Since pseudocapacitors rely on surface redox processes wherein the active species can be elec-troadsorbed/desorbed with charge transfer near the surface, 3D hierarchical porous architectures and ultrathin graphene nanosheets decorated with tiny, yet numerous PMo_{12} clusters endow rGO–PMo_{12} with an excellent volumetric capacitance of over 3.18 F cm^{-3} which is much larger than those values for Rgo (1.10 F cm^{-3}). But in addition to extra

capacitance PMo_{12} also provides an opportunity for an increased voltage window. Indeed, the adsorbed PMo_{12} features an overpotential of 0.3 V on the positive side which allows for the realization of a broad voltage of 1.6 V for the all-solid state rGO–PMo_{12} supercapacitor with an acidic electrolyte. This value is well beyond the thermodynamic stability window of water (1.23 V), and amazingly comparable to asymmetric systems. The combination of extra capacitance and widened voltage window of this truly synergic electrode material allows for attaining a remarkable energy density of 1.04 mW h cm^{-3}.

In addition, and for the first time, we have extended our work dedicating earnest efforts to investigate the effect of addition of redox-active species (hydroquinone in this particular case) in the gel-electrolyte to further improve the performance of rGO– PMo_{12} solid-state symmetric capacitors.

Experimental

Synthesis of reduced graphene oxide (rGO) and rGO–PMo12 hybrids

Graphene oxide (GO) was synthesized from natural graphite using the modified Hummers method. Briefly, 2.5 g of NaNO3 and 125 ml of H2SO4 were added to 2.5 g of graphite and stirred for 30 min in an ice bath. 12.5 g of $KMnO_4$ was added to the resulting solution, and then the solution was stirred at 50 ^{o} C for 2 h. 500 ml of deionized water and 15 ml of H_2O_2 (35%) were then slowly added to the solution, and the solution was washed with dilute HCl. Further, the GO product was washed again with 250 ml of concentrated HCl (37%). The reduced graphene oxide (rGO) was prepared by high temperature treatment of the GO sample at 800 ^{o} C under nitrogen for 1 h.

In the second step, we prepared hybrid materials based on rGO and phosphomolybdic acid (rGO–PMO_{12}). Briefly, 0.25 g of rGO was dispersed in 100 ml of deionized water with a probe sonicator (of power 1500 watt) for 1 h. We varied the concentration of phosphomolybdic acid

($H_3PMo_{12}O_{40}.3H_2O$, (PMo_{12})) from 1 mM, 2 mM, 5 mM, 10 mM and 15 mM. It is observed that with an increase in concentration from 1 mM to 10 mM, the loading of PMo_{12} on rGO increases which slightly decreases or saturates with further increase in concentration (15 mM). This might be attributed to the sufficient anchoring of PMo_{12} on the rGO surface till the concentration of 10 mM phosphomolybdic acid ($H_3PMo_{12}O_{40}3H_2O$, (PMo_{12})) due to limited functional groups at the surface of rGO. Thus, the maximum and uniform loading of 0.28 mmol PMo_{12} per gram of rGO was observed for 10 mM phosphomolybdic acid. Hence, 10 mM of phosphomolybdic acid ($H_3PMo_{12}O_{40}.3H_2O$, (PMo_{12})) was added to the above pre-sonicated 100 ml rGO dispersion. This suspension was further sonicated (bath sonicator 200 watt) for 5 h and kept at room temperature for 24 h. Afterwards, the product was filtered off and dried in a vacuum oven at 80 ^{o} C overnight.

Electrochemical measurements

To measure the electrochemical performances, 85% of the active material (rGO or rGO–PMo_{12}) was mixed with 10% PVDF as the binder and 5% acetylene black. A few drops of N-methyl-2-pyrrolidone (NMP, solvent) were added and the mixture was homogenized using a mortar to get a uniform paste. Finally the paste was applied on a commercial flexible carbon cloth which was further used as an SC electrode. All-solid state symmetric supercapacitors were fabricated using Swagelok® cells with two rGO–PMo_{12} electrodes of the same mass and H_2SO_4/PVA gel electrolytes assembled under pressure. All electrochemical measurements (cyclic voltammetry (CV) and galvanostatic charge–discharge techniques) were carried out using a Biologic VMP3 potentiostat.

Results and discusion

A series of morphological characterizations have been carried out to confirm the effective anchoring of PMo_{12} onto the surface of 3D open porous rGO nanosheets. Fig. 2(a and b) present SEM images of rGO and rGO–PMo_{12} hybrid materials, respectively. First, it can be seen that rGO exhibits a 3D open-porous architecture composed of ultrathin nanosheets conforming to an electronically conductive framework which is highly beneficial for enhancing the electron transport while maintaining good ionic conductivity. Furthermore, it is important to note that rGO preserves its 3D open porous structure even after heavy depo- sition of PMo_{12} clusters (see Fig. 2(b)). EDS mapping of the rG-PMo_{12} hybrid sample was carried out and is shown in Fig. 2(c) which clearly confirms that the PMo_{12} 1 nm clusters are homogeneously distributed and efficiently anchored onto the rGO nanosheets (see ESI Fig. S1†). Fig. 2(d) shows a HR- TEM image of the rGO–PMo_{12} sample in which PMo_{12} clusters are clearly observed as tiny black specks. In order to get more insight about the distribution of PMo_{12} on rGO nanosheets, STEM analysis was carried out and is displayed in Fig. 2(e and f). It is unambiguously seen that the surface of rGO nanosheets is blank and free from tiny spots (Fig. 2(e)), while in great contrast the surface of the rGO–PMo_{12} hybrid is abundantly decorated with nanometer-sized PMo_{12} dots (Fig. 2(f)) (see also EDS mapping with STEM in ESI Fig. S2†). It should also be noted that the PMo_{12} clusters are evenly distributed on the rGO surface without any apparent agglomeration.

It is very important to note the utterly dispersed nature of the electroactive centers in this hybrid material. PMo_{12} clusters have all twelve Mo moieties on the surface of the 1 nm-sized cluster (there is no “bulk”). Since the pseudo-capacitive energy storage mechanism is based on surface redox processes where energy storage is due to charge transfer near the surface, the present hybrid configuration is ideal for electrode–electrolyte surface polarization. Indeed, this unique rGO–PMo_{12} hybrid

combines a conducting 3D open porous nanoarchitecture with anchored PMo_{12} redox active clusters unlike oxide quantum dots, thus providing an optimal starting point from a structural point of view for high energy storage.

Fig. 3(a) shows XRD patterns of rGO and rGO–PMo_{12} hybrid materials. Both materials show two distinct peaks at 25.6^{o} and 42.5^{o} which are characteristic of carbon materials and correspond to the (002) and (001) planes respectively.[17] No peak associated with the crystal structure of PMo_{12} is observed in good agreement with the total dispersion of the molecular PMo_{12} clusters on rGO and confirming the absence of any significant packing of the clusters. On the other hand, both the (001) peaks are broader for the hybrid material, indicating a poorer long-range order with respect to the parent rGO induced by the adsorption of the inorganic clusters. Fig. 3(b) shows the full XPS spectra of rGO and rGO–PMo_{12} samples which clearly indicate the presence of carbon (284.5 eV, C 1s) and oxygen (533.5 eV, O 1s) in both spectra with an additional peak at 232.7 eV (3d) in the rGO–PMo_{12} sample corresponding to molybdenum. Close inspection of C 1s spectra (see Fig. 3(c)) shows a significant decrease in the peak intensity and a slight shift towards the low binding energy for the rGO–PMo_{12} sample which strongly supports the XRD results. Furthermore, the presence of Mo 3d peaks at 232.3 eV (Mo $3d_{3/2}$) and 235.4 eV (Mo $3d_{5/2}$) unambiguously confirm the presence of PMo_{12} in the rGO–PMo_{12} hybrid with most of the molybdenum in the Mo(VI) formal oxidation state (Fig. 3(d)). Thus, formation of the rGO–PMo_{12} hybrid is positively confirmed.[18,19] A high surface area with an open-pore structure is one of the keys to high performance hybrid electrode materials for energy storage. In this sense, nitrogen adsorption–desorption curves and the corresponding pore size distribution plots for rGO and rGO–PMo_{12} samples are shown in Fig. 4(a and b). The shape of the hysteresis loop is characteristic of mesoporous materials. BET analyses of these data showed that both the samples rGO and rGO–PMo_{12}

exhibit high surface areas of 242 $m^2\ g^{-1}$ and 231 $m^2\ g^{-1}$, respectively. The slight decrease in the active surface of the rGO–PMo_{12} sample is attributed to the inclusion of the PMo_{12} nanoparticles, that contribute heavily to the total mass of the hybrid. When PMo_{12} adsorbs on the surface of graphene, they try to cover the macropores of the host material and make them narrower (micropores) which actually do not affect the surface area, but due to the high weight of POMs, a slight decrease is noticed. Even with this slight decrease the specific BET surface area of rGO–PMo_{12} is considerably larger than many recently reported carbon/metal oxide hybrid mate- rials.[20,21] Also, Chen et al.[22] prepared a novel nanohybrid based on single-walled carbon nanotubes (SWCNTs) with a poly- oxomethalate $(TBA)_5[PV_2^{V}Mo_{10}^{VI}O_{40}]$ (TBA-PV_2Mo_{10}, TBA: $[(CH_3(CH_2)_3)_4N]^+$, tetra-n-butyl ammonium) and reported a maximum BET surface area of 71 $m^2\ g^{-1}$.

The mesoporous nature of both rGO and rGO–PMo_{12} samples can be further confirmed by pore-size distribution analysis as seen from the insets of Fig. 4(a and b), indicating a pore size range of 2–8 nm. Interestingly, the pore volume of rGO does increase from 0.10 $cm^3\ g^{-1}$ to 0.14 $cm^3\ g^{-1}$ after anchoring the PMo_{12} inorganic cluster, which is favorable for ion insertion/de-insertion into the electrode material during the electrochemical operation. It is interesting and justifies our statement that, the adsorption of PMo_{12} turns the macro- porosity of rGO–PMo_{12} into microporosity as observed with the decrease in the peak intensity at ~7.70 nm and with a slight increase in that at ~3.48 nm (insets of Fig. 4(a) and b).

Electrochemical performance of all-solid-state rGO–PMo12 Symmetric cells

In order to investigate the electrochemical performances of rGO and rGO–PMo_{12} hybrid electrodes, symmetric cells were assembled by sandwiching an H_2SO_4/PVA gel-electrolyte between two identical electrodes (either rGO or rGO–PMo_{12}). Fig. 5(a and b) show cyclic voltammetry curves, at various scanning rates, for rGO and rGO–PMo_{12} symmetric cells, respectively. The shape of CV curves for the rGO-based symmetric cell is ideally rectangular confirming the contribution from the electric double layer capacitance (EDLC). On the other hand, quasi-rectangular CV curves are observed for the rGO–PMo_{12} symmetric cell, with various broad redox waves from PMo_{12} overlapping with a rectangular (capacitive) envelope. This CV structure ratifies the coexistence of both charge- storing mechanisms, faradaic and EDLC. Moreover, even at a scan rate as high as 100 mV s^{-1}, the CV curve still shows obvious redox peaks in the charge and discharge processes, indicating the superior high-rate capability of rGO–PMo_{12} symmetric cells for fast charge and discharge. Fig. 5(c and d) present galvanostatic charge/discharge (CD) curves for rGO and rGO–PMo_{12} based symmetric cells at different current densities, respectively. The shapes of the CD curves for both symmetric cells (rGO and rGO–PMo_{12}) are considerably different which strongly support the CV results, further confirming the presence of both charge-storing mechanisms. A common and impressive fact about both cells is a very small initial voltage drop with nearly symmetric discharge curves suggesting a rapid I–V response and good electrochemical reversibility. The synergic combination of EDLC (rGO) and faradaic (redox active, PMo_{12}) activities is further confirmed from the shape of the CD curves.

The rGO/PMo_{12} hybrid electrode material showed excellent electrochemical properties due to the proper hybridization of faradaic components (PMo_{12}) and capacitor components (rGO) in single electrodes. In this hybrid electrode, the capacitor component is first charged by electrostatic forces in the initial state until the electrode potential reaches the redox reaction potential of the faradaic (PMo_{12}) component. Then the faradaic component (PMo_{12}) is charged through the redox reaction

while maintaining the potential of the hybrid electrode, until the faradaic component reaches its full-charge state. After the full charge of the faradaic component, the capacitor component is charged again until the maximum potential of the hybrid electrode is reached. Hence the total charge stored in the hybrid electrode is due to both components (PMo_{12} and rGO).

Fig. 6 summarizes the effect of the PMo_{12} attachment on the electrochemical performances of rGO in all-solid-state symmetric cells. Fig. 6(a) shows the CV curves of rGO and rGO– PMo_{12} symmetric cells at a constant scan rate of 20 mV s^{-1}. It is worth noting the extensive increase in the current density for the cell with two rGO–PMo_{12} hybrid electrodes along with the extension of 0.3 V compared to that of the symmetrical rGO cell. Furthermore, as seen in Fig. 6(b), the discharging time for the rGO–PMo_{12} symmetric cell is substantially longer than that for the rGO-based symmetric cell, indicating a significantly larger specific capacitance. Furthermore, the allowed operational voltage window is increased from 1.3 V for the rGO cell to 1.6 V for the rGO–PMo_{12} cell, which leads to an increased energy density. This significant improvement in the overall electrochemical performance should be attributed to the synergic effect between rGO (EDLC) and PMo_{12} (faradaic) in the hybrid electrodes. It should be noted that all electrochemical parameters were calculated by standard equations (see ESI S3†). Fig. 6(c) shows the variation of volumetric capacitances of rGO and rGO–PMo_{12} based symmetric cells as a function of scan rates. The rGO–PMo_{12} symmetric cell provides a volumetric capacitance of 3.18 F cm^{-3} (278 mF cm^{-2} and 51.2 F g^{-1} for a total mass loading of both electrodes 6.8 mg) and 1.09 F cm^{-3} (96 mF cm^{-2} and 17.7 F g^{-1}) at scan rates of 5 and 100 mV s^{-1}, respectively. This represents a much higher capacitance than the rGO symmetric cell (1.10 F cm^{-3} (96 mF cm^{-2} and 36.8 F g^{-1} for the total mass loading of both electrodes 3.1 mg) and 0.39 F cm^{-3} (34 mF cm^{-2} and 13.1 F g^{-1}) at scan rates of 5 and 100 mV s^{-1}, respectively). This enormous

increase of the specific capacitance is due to the faradaic contribution of PMo_{12} in the nanohybrid. Remarkably, up to 35% (for rGO) and 34% (for rGO–PMo_{12}) of the capacitance is retained when the scan rate is increased from 5 to 100 mV s^{-1}, indicating very good high-rate performance for these symmetric devices (ESI S4†). As expected, the specific capacitances decrease with increase in the scan rate which might correspond to diffusion limitations. The values reported here are considerably higher than those for other symmetric and even asymmetric cells not only of POM- based electrodes[22–26] but also metal oxides electrodes with polymer gel-electrolytes.[27–32] A summary of supercapacitive values of POM and metal oxide-based electrodes are tabulated in ESI S5.† Fig. 6(d) presents the volumetric power and energy density values of rGO and rGO–PMo_{12} symmetric cells using equations from Chen et al.[32b] It can be observed in the Ragone plots that the rGO–PMo_{12} symmetric cell delivers a higher volumetric energy than rGO symmetric cells. The maximum volumetric energy of 1.07 mW h cm^{-3} can be obtained from the rGO–PMo_{12} symmetric cell at a power of 12 mW cm^{-3}, whereas the volumetric energy of the rGO symmetric cell is around 0.22 mW h cm^{-3} at a power of 12 mW cm^{-3}. Even at a high power density of 188 mW cm^{-3}, the rGO–PMo_{12} symmetric cell stil provides a higher energy density of 0.25 mW h cm^{-3}. These results demonstrate that the rGO–PMo_{12} symmetric cell with the polymer gel-electrolyte is a strong contending design for high power as well as high energy supercapacitor applications. The results obtained here with polymer gel-electrolytes are far better than those for liquid electrolytes. The whole credit for this extraordinary performance goes to smartly anchored PMo_{12} nanodots as well as to the unique cell design combining both EDLC and faradaic storage mechanisms at each electrode of the device. This symmetric configuration also eliminates the use of complex chemistries involved in using

different electrode materials (asymmetric cells) as well as complications in balancing the charge (or mass) of both electrodes.

The hybrid electrode is bound to have improved power densities compared to those of typical pseudocapacitors or battery electrodes due to its structural characteristics. This is so because the capacitor component, which can also store electrochemical energy by electrostatic force, enhances the electron transfer to the PMo_{12} component in the hybrid electrode system, causing a better charge transfer reaction at high rates. The electrochemical performance of the hybrid electrode material is based on the hybridization and surrounding characteristics of both components. Therefore, proper composition and morphological structure are key factors to realize the full potential of hybrid electrode materials compared to conventional electrode materials.

Effects of hydroquinone doping in gel-electrolytes

The electrolyte is not the least important factor in determining the performance of a supercapacitor device. Among different electrolytes, solid state gel-electrolytes present several advantages: (i) they conduct ions via voids in their gel network reaching conductivities comparable to aqueous electrolytes, (ii) their use solves the issue of electrolyte leakage during device fabrication or operation and (iii) they work both as a separator and as electrolyte. However, they still have room for improvement. Indeed, recent reports[33] have shown how the addition of a redox active species in a liquid electrolyte helps to improve the overall device performance,[34,35] in particular conducting polymers.[34] Inspired from these works, we are presenting the first successful example to further improve the performance of an rGO–PMo_{12} symmetric cell with redox-active species (hydroquinone) doped into a PVA/H_2SO_4 gel-electrolyte. The quinone/hydroquinone (Q/HQ) redox couple of p-benzoquinone is highly reversible and undergoes a 2-electron redox process. The hybrid

gel-electrolyte was prepared by doping the conventional PVA/H_2SO_4 polymer gel-electrolyte solution with different concentrations of hydro- quinone (0.1, 0.2 and 0.3 M). Fig. 7(a–c) shows CV curves of rGO–PMo_{12} symmetric cells with an HQ doped gel-electrolyte of different concentrations at various scan rates. Remarkably, all CV curves deviate from ideal rectangular shapes and show intense redox peaks which result in higher capacity. These characteristics obviously originate from Q/HQ redox reactions upon the addition of the redox-active p-benzoquinone species in the gel-electrolyte. The additional protons introduced by hydroquinone/quinone couples provide more reaction sites for fast and reversible redox reactions which radically increase the electrochemical response of the devices.[35] It is noteworthy that the hydroquinone (HQ) not only provides extra redox activity but also additional protons and improved ionic conductivity to the polymer gel-electrolyte.

The integrated area of the CV loops of rGO–PMo_{12} cells reaches a maximum for a 0.2 M HQ doped gel-electrolyte and decreases with further increase in the doping concentration of HQ (ESI S6†). A similar trend is observed in the CD tests for rGO–PMo_{12} cells, where the charge and discharge times increase up to the 0.2 M HQ doped electrolyte and start to decrease for further increase in the concentration of HQ (see ESI S7†). Fig. 7(d) is the summary of volumetric capacitance vs. scan rate of rGO–PMo_{12} cells with different HQ concentrations. It is clearly shown that the rGO–PMo_{12} cell with the 0.2 M HQ doped gel-electrolyte exhibits the highest volumetric capacitance which decreases with further increase in HQ concentration. The volumetric capacitances achieved for rGO–PMo_{12} with the 0.2 M HQ gel-electrolyte is 4.8 F cm^{-3} (419 mF cm^{-2}) and 1.52 F cm^{-3} (133 mF cm^{-2}) at scan rates of 5 mV s^{-1} and 100 mV s^{-1}, respectively which are considerably higher than that obtained without HQ in the gel-electrolyte. Even at high HQ concentration (0.3 M), the cell exhibits a capacitance of 4.09 F cm^{-3} (358 mF cm^{-2}) at 5 mV s^{-1} which is still significantly higher than

that of the rGO–PMo_{12} cell with an un-doped gel-electrolyte. As it could be expected, all capacitances decrease with increasing scan rates due to the limitations of diffusion and transpor of electrolyte ions at higher scan rates.

CD measurements for the rGO–PMo_{12} symmetric cell with the 0.2 M HQ doped electrolyte at different current densities were carried out and are presented in Fig. 7(e). As expected, the shapes of the CD curves are completely deviated from the ideal triangular shape which supports the CV results and confirms the redox contribution from HQ.

Thus, double hybridization, namely, that of hybrid electrodes and that of a hybrid electrolyte, effectively work together to enhance the overall device performance. Fig. 7(f) shows the variation of volumetric capacitances with the current density of the rGO–PMo_{12} cell for different concentrations of HQ. It is evidenced that with an increase in HQ concentrations the volumetric capacitance of the rGO–PMo_{12} cell increases till 0.2 M HQ and then decreases for 0.3 M HQ. The capacity retention with a current density of rGO–PMo_{12} cells was calculated for different HQ doping. The capacity retention of the rGO–PMo_{12} cell for HQ doped gel-electrolytes is more than 40% which is considerably higher than that for the un-doped electrolyte cell (29%). This further proves the excellent potential for high-rate performance of the hybrid electrode, which the hybrid electrolyte helps to fulfill.

Both the volumetric and gravimetric energy/power densities are presented in the Ragone plots of Fig 8(a and b), respectively. The volumetric energy densities of the rGO–PMo_{12} cell for different HQ doping concentrations are 1.18 mW h cm^{-3} (12 W h kg^{-1}), 1.70 mW h cm^{-3} (17.20 W h kg^{-1}) and 1.59 mW h cm^{-3} (16.21 W h kg^{-1}) at a constant power density of 12 mW cm^{-3} (127.1 W kg^{-1}) for 0.1 M, 0.2 M and 0.3 M HQ concentrations, respectively. More interestingly, even at a high power density of 118–129 mW cm^{-3} (1.2–1.3 kW kg^{-1}), the rGO–PMo_{12} cell with the hybrid gel-electrolyte

exhibits energy densities in the range of 0.3–0.43 mW h cm^{-3}, confirming the great potential for application in high performance devices. These values are considerably higher than the values reported for recent solid state symmetric and even asymmetric devices.[27–29,31,32,36–38]

These results show a considerable enhancement in the capacity of supercapacitors by just adding one redox-active component to the conventional electrolyte. The capacitance retention of the rGO–PMo_{12} symmetric cell measured in the cycling charge–discharge test at a current density of 12.7 mA cm^{-2} in redox-active electrolyte is shown in Fig. 8(c). It is noticed that the cycling stability of the rGO–PMo_{12} based pseudocapacitors in the redox-active electrolytes is not as good as that in the conventional electrolyte, which is due to the intensive redox reactions introduced by the redox-active electrolytes. Although the degradation of capacitance is a common problem in pseudo-capacitive materials, our rGO–PMo_{12} hybrid cell exhibits capacity retention in the range of 89–95% with the redox-active (HQ) electrolyte. This high cycling stability is mainly contributed by the synergetic effect of rGO (EDLC) and PMo_{12} (redox-active molecular clusters). Chronoamperometry (CA) is another electrochemical technique completely different than cyclic voltammetry in which the capacitance is either dependent on the scan rate or current density. On the other hand, in CA, the potential of the working electrode is stepped and the resulting current from faradaic processes occurring at the electrode (caused by the potential step) is monitored as a function of time. After a 20 min conditioning period (full discharge to 0 V), the cell was charged to 0.4, 0.2 and 0.1 V for 1 min, as shown in Fig. 8(d). While charging was associated with additional leakage current, the integration of the discharge current with time directly yields the charge for a given cell potential. As found by chronoamperometry, the intrinsic equilibrium capacitance of the rGO–PMo_{12} cell with the 0.2 M HQ doped gel- electrolyte, is yet higher than the capacitance derived from CV and CD methods

(ESI S6†). When compensating for the leakage current, the coulombic efficiency of the rGO–PMo_{12} cell was observed to be 95.7% which is comparable to that from CD curves.

In order to show practical applicability of the rGO–PMo_{12} cell with the redox-active electrolyte a demonstration with LEDs is provided. Strikingly, the word "NEO" made with 31 (thirty-one) LEDs is lit by a single symmetric device for almost 2 minutes after a short full-charging time of rv30 s, indicating a sustained energy output founded on rapid charge (see Fig. 9). These excellent performances are made possible by the unique combination of hybrid electrodes with a hybrid electrolyte (doped with redox-active species) which includes the following features: (1) full advantage of two charge storing mechanisms i.e. EDLC (rGO) and faradaic (PMo_{12}), (2) rGO nanosheets create fast electronic and ionic conducting channels, (3) tiny, yet strongly anchored PMo_{12} clusters provide a high concentration of redox active sites which contributes to the high capacitance, (4) a unique cell design in which the combination of pseudo- capacitors and EDLCs at both ends (rGO–PMo_{12}) extends the voltage window to 1.6 V, resulting in an improved energy density, and (5) last but not least, doping of the gel-electrolyte with redox-active HQ provides extra protons and improved ionic conductivity as well as additional faradaic active sites for energy storage. Indeed, HQ doping provides a molecular species which can be reversibly oxidized at the positive electrode during charge counterbalancing the simultaneous faradaic reduction of PMo_{12} at the negative electrode in a battery-like arrangement adding further energy density to the device.

Conclusions

We have implemented a double hybridization approach in solid state supercapacitors comprising (i) the preparation of hybrid electrodes by anchoring PMo_{12} redox-active clusters onto rGO nanosheets and (ii) the use of a hybrid gel-electrolyte formulation introducing redox-active hydroquinone species to a conventional H_2SO_4 electrolyte. The rGO–PMo_{12} symmetric cell with the

conventional gel-electrolyte shows a significant improvement in the performance, extending the potential window by 0.3 V with an energy density of 1.07 mW h cm^{-3} Furthermore, for the first time a redox-active species (HQ) doped. solid-state gel electrolyte was used with an rGO–PMo_{12} hybrid supercapacitor which significantly enhanced the overall performance of the device. Impressively, an excellent increase in the device performance (energy density of 1.7 mW h cm^{-3}) with the redox-active electrolyte has been achieved. These encouraging findings prove the great potential of this double hybrid approach with rGO–PMo_{12} hybrid electrodes and hybrid electrolytes for the design of high energy density, high power density, and long cycle life energy storage systems.

Acknowledgements

The authors appreciate the award to DPD with the support of the Secretary for Universities and Research of the Ministry of Economy and Knowledge of the Government of Catalonia and the Co-fund programme of the Marie Curie Actions of the 7^{th} R&D Framework Programme of the European Union". This work was funded by the Spanish Ministerio under grant MAT2012-39199-C02-01. ICN2 acknowledges support of the Spanish MINECO through the Severo Ochoa Centers of Excellence Program under Grant SEV-2013-0295.

References

1 P. Simon and Y. Gogotsi, Nat. Mater., 2008, 7, 845–854.

2 (a) D. P. Dubal, O. Ayyad, V. Ruiz and P. Gomez-Romero, Chem. Soc. Rev., 2015, 44, 1777–1790; (b)
D. P. Dubal, J. G. Kim, Y. Kim, R. Holze, C. D. Lokhande and W. B. Kim, Energy Technol., 2014, 2,
325–341.

3 D. Pech, M. Brunet, H. Durou, P. Huang, V. Mochalin, Y. Gogotsi, P. L. Taberna and P. Simon, Nat
Nanotechnol., 2010, 5, 651–654.

4 P. Simon, Y. Gogotsi and B. Dunn, Science, 2014, 343, 1210– 1211.

5 (a) G. Yu, X. Xie, L. Pan, Z. Bao and Y. Cui, Nano Energy, 2013, 2, 213–234; (b) D. P. Dubal, R. Holze
and P. Gomez-Romero, Sci. Rep., 2014, 4, 7349.

6 (a) J. Suarez-Guevara, V. Ruiz and P. Gomez-Romero, J. Mater. Chem. A, 2014, 2, 1014–1021; (b) D
P. Dubal, D. Aradilla, G. Bidan, P. Gentile, T. J. S. Schubert, J. Wimberg, S. Sadki and P. Gomez-
Romero, Sci. Rep., 2015, 5, 09771.

7 D. P. Dubal, P. Gomez-Romero, B. R. Sankapal and R. Holze, Nano Energy, 2015, 11, 377–399.

8 A. Muller, E. Krickemeyer, J. Meyer, H. Bogge, F. Peters, W. Plass, E. Diemann, S. Dillinger, F.
Nonnenbruch, M. Randerath and C. Menke, Angew. Chem., Int. Ed., 1995, 34, 2122–2124.

9 A. Muller, E. Beckmann, H. Bogge, M. Schmidtmann and A. Dress, Angew. Chem., Int. Ed., 2002,
41, 1162–1167.

10 P. Gomez-Romero and M. Lira-Cantu´, Adv. Mater., 1997, 9, 144–147.

11 J. Vaillant, M. Lira-Cantu, K. Cuentas-Gallegos, N. Casan˜- Pastor and P. Gomez -Romero, Prog
Solid State Chem., 2006, 34, 147–159.

12 J. Suarez -Guevara, V. Ruiz and P. Gomez-Romero, Phys. Chem. Chem. Phys., 2014, 16, 20411–
20414.

13 A. Cuentas-Gallegos, R. Martinez-Rosales, M. Baibarac, P. Gomez-Romero and M. E. Rincon,
Electrochem. Commun., 2007, 9, 2088–2092.

14 T. Akter, K. W. Hu and K. Lian, Electrochim. Acta, 2011, 56, 4966–4971.

15 V. Ruiz, J. Suarez-Guevara and P. Gomez-Romero, Electrochem. Commun., 2012, 24, 35–38.

16 F. Wang, S. Xiao, Y. Hou, C. Hu, L. Liu and Y. Wu, RSC Adv., 2013, 3, 13059–13084.

17 H. Kim, K. Y. Park, J. Hong and K. Kang, Sci. Rep., 2014, 4, 5278.

18 A. Ma, X. Zhang, Z. Li, X. Wang, L. Ye and S. Lin, J. Electrochem. Soc., 2014, 161, F1224–F1230.

19 G. Bajwa, M. Genovese and K. Lian, ECS J. Solid State Sci. Technol., 2013, 2, M3046–M3050.

20 Y. Ji, L. Huang, J. Hu, C. Streb and Y. F. Song, Energy Environ. Sci., 2015, 8, 776–789.

21 W. Wei, X. Cui, W. Chen and D. G. Ivey, Chem. Soc. Rev., 2011, 40, 1697–1721.

22 H. Y. Chen, R. Al-Oweini, J. Friedl, C. Y. Lee, L. Li, U. Kortz, U. Stimming and M. Srinivasan, Nanoscale, 2015, 7, 7934–7941.

23 M. Skunik, M. Chojak, I. A. Rutkowska and P. J. Kulesza, Electrochim. Acta, 2008, 53, 3862–3869.

24 G. M. Suppes, C. G. Cameron and M. S. Freund, J. Electrochem. Soc., 2010, 157, A1030–A1034.

25 P. Gomez-Romero, M. Chojak, A. Cuentas-Gallegos, J. A. Asensio, P. J. Kulesza, N. Casan-Pastor and M. Lira- Cantu, Electrochem. Commun., 2003, 5, 149–153.

26 A. Cuentas-Gallegos, M. Lira-Cantu, N. Casan-Pastor and P. Gomez-Romero, Adv. Funct. Mater., 2005, 15, 1125– 1133.

27 X. Lu, Y. Zeng, M. Yu, T. Zhai, C. Liang, S. Xie, M. Balogun and Y. Tong, Adv. Mater., 2014, 26, 3148–3155.

28 P. Yang, X. Xiao, Y. Li, Y. Ding, P. Qiang, X. Tan, W. Mai, Z. Lin, W. Wu, T. Li, H. Jin, P. Liu, J. Zhou, C. P. Wong and Z. L. Wang, ACS Nano, 2013, 7, 2617–2626.

29 X. H. Lu, G. M. Wang, T. Zhai, M. H. Yu, S. L. Xie, Y. C. Ling, C. L. Liang, Y. X. Tong and Y. Li, Nano Lett., 2012, 12, 5376–
5381.

30 M. F. El-Kady, V. Strong, S. Dubin and R. B. Kaner, Science, 2012, 335, 1326–1330.

31 W. Zilong, Z. Zhu, J. Qiu and S. Yang, J. Mater. Chem. C, 2014, 2, 1331–1336.

32 (a) X. Lu, M. Yu, G. Wang, T. Zhai, S. Xie, Y. Ling, Y. Tong and Y. Li, Adv. Mater., 2013, 25, 267–272; (b) G. Z. Chen, Prog. Nat. Sci. Mat. Int., 2013, 23, 245–255.

33 F. Beguin, V. Presser, A. Balducci and E. Frackowiak, Adv. Mater., 2014, 26, 2219–2251.

34 W. Chen, R. B. Rakhi and H. N. Alshareef, J. Phys. Chem. C, 2013, 117, 15009–15019.

35 S. Roldan, C. Blanco, M. Granda, R. Menendez and

R. Santamaria, Angew. Chem., Int. Ed., 2011, 50, 1699–1701.

36 X. Xiao, X. Peng, H. Jin, T. Li, C. Zhang, B. Gao, B. Hu, K. Huo and J. Zhou, Adv. Mater., 2013, 25, 5091–5097.

37 L. Y. Yuan, X. H. Lu, X. Xiao, T. Zhai, J. J. Dai, F. C. Zhang, B. Hu, X. Wang, L. Gong, J. Chen, C. G. Hu, Y. X. Tong, J. Zhou and Z. L. Wang, ACS Nano, 2012, 6, 656–661.

38 X. Lu, M. Yu, T. Zhai, G. Wang, S. Xie, T. Liu, C. Liang, Y. Tong and Y. Li, Nano Lett., 2013, 13, 2628–2633.

Figures

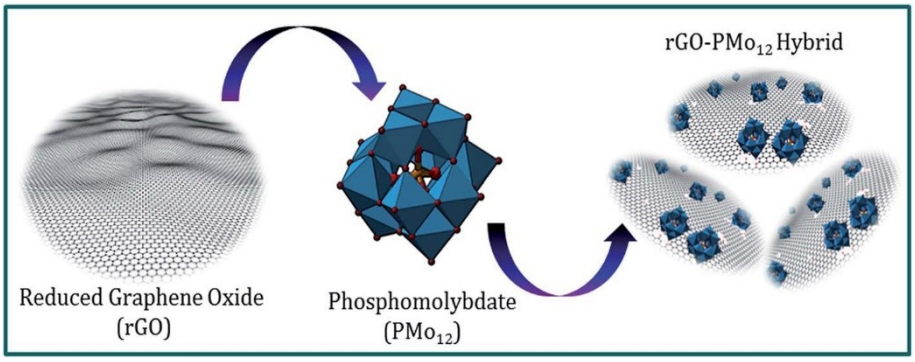

Fig. 1 Schematic illustration of the steps involved in the synthesis of reduced graphene oxide (rGO) and the phosphomolybdate (PMo_{12}) hybrid material (rGO-PMo_{12}) by a simple chemical technique.

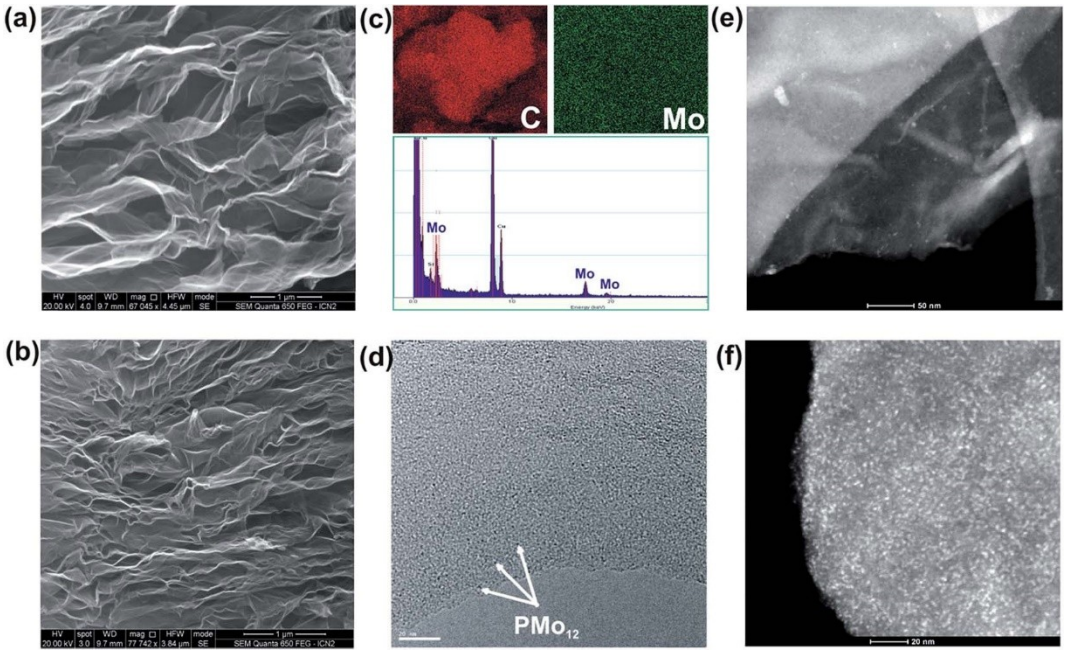

Fig. 2 (a and b) SEM images of rGO and rGO–PMo_{12} hybrid materials, respectively, (c) EDS mapping of the rGO–PMo_{12} hybrid sample, (d) HR- TEM image of the rGO–PMo_{12} sample, and (e and f) STEM images of rGO and rGO–PMo_{12} hybrid samples, respectively.

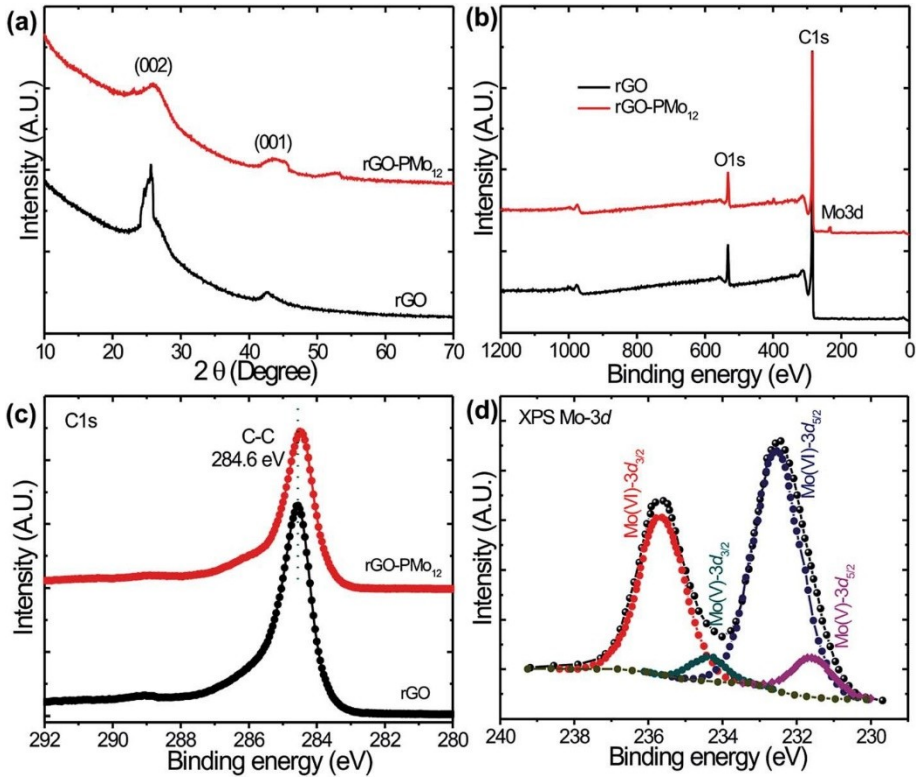

Fig. 3 (a) XRD patterns of rGO and rGO–PMo_{12} hybrid materials, (b) full XPS spectra of rGO and rGO–PMo_{12} samples, and (c and d) core-level XPS spectra of C 1s and Mo 3d of the rGO–PMo_{12} sample, respectively.

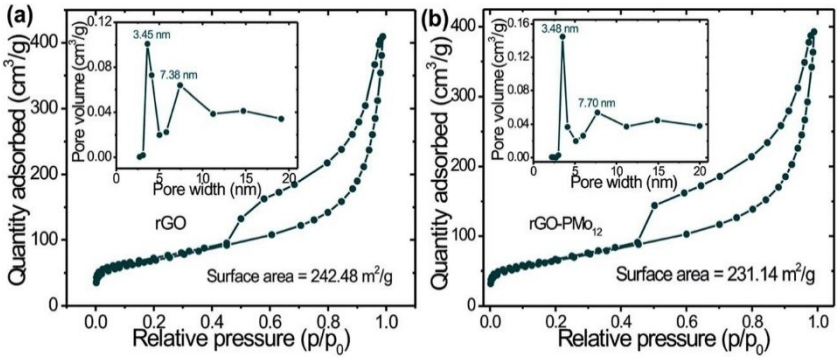

Fig. 4 (a and b) Nitrogen adsorption–desorption curves with the corresponding pore size distribution plots for rGO and rGO–PMo_{12} samples, respectively.

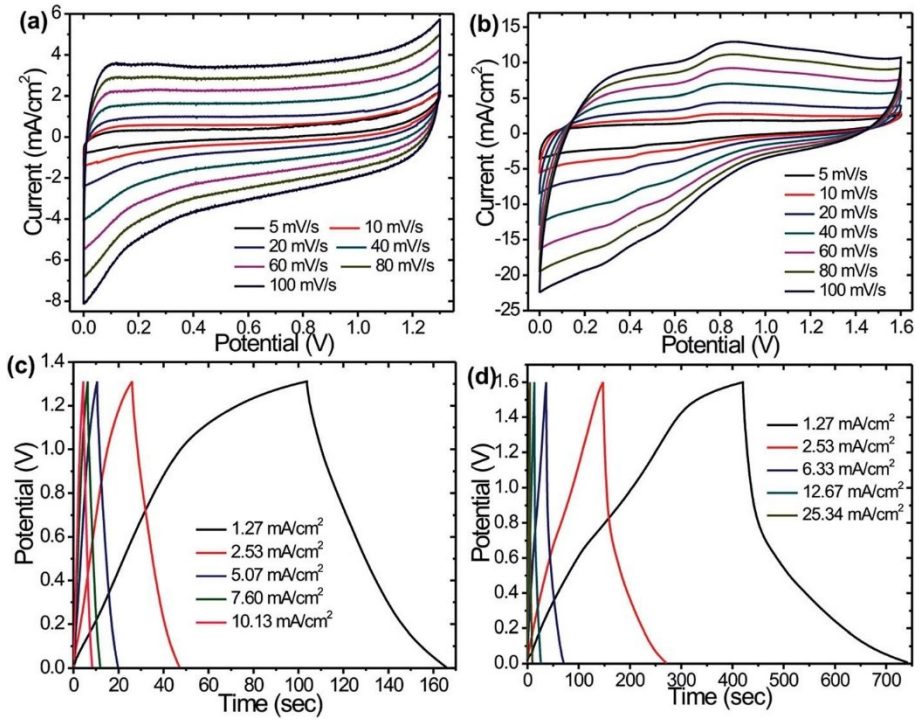

Fig. 5 (a and b) Cyclic voltammetry (CV) curves of rGO and rGO–PMo_{12} symmetric cells at different scanning rates, respectively, and (c and d) galvanostatic charge/discharge (CD) curves of rGO and rGO–PMo_{12} based symmetric cells at different current densities, respectively.

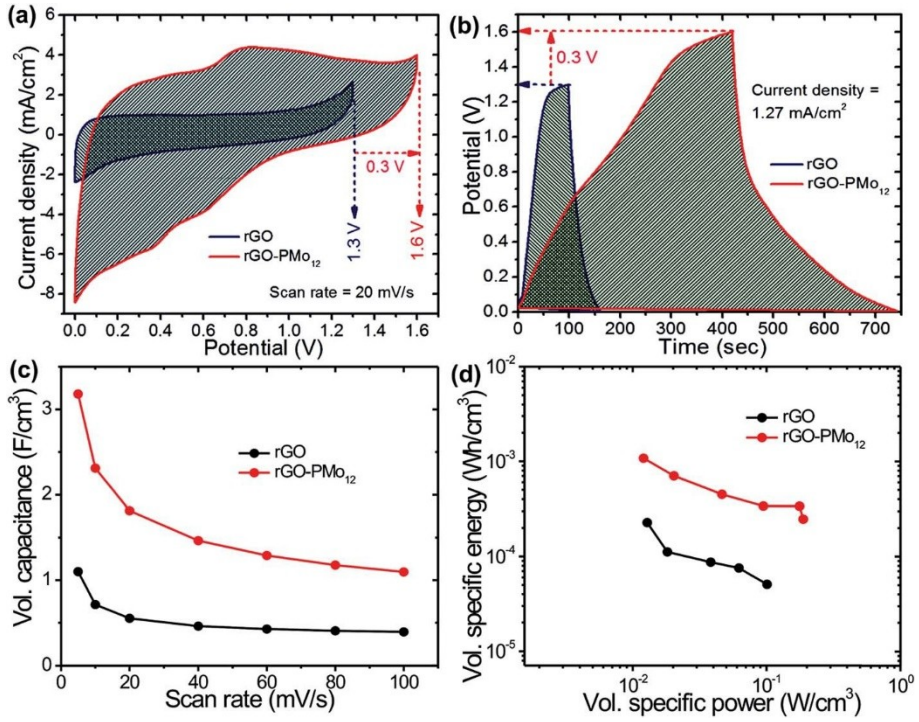

Fig. 6 (a) CV curves and (b) CD curves of rGO and rGO–PMo_{12} symmetric cells at a scan rate of 20 mV s^{-1} and a current density of 1.27 mA cm^{-2}, respectively, (c) variation of volumetric capacitances of rGO and rGO–PMo_{12} based symmetric cells as a function of scan rates, and (d) the volumetric power and energy density values of rGO and rGO–PMo_{12} symmetric cells.

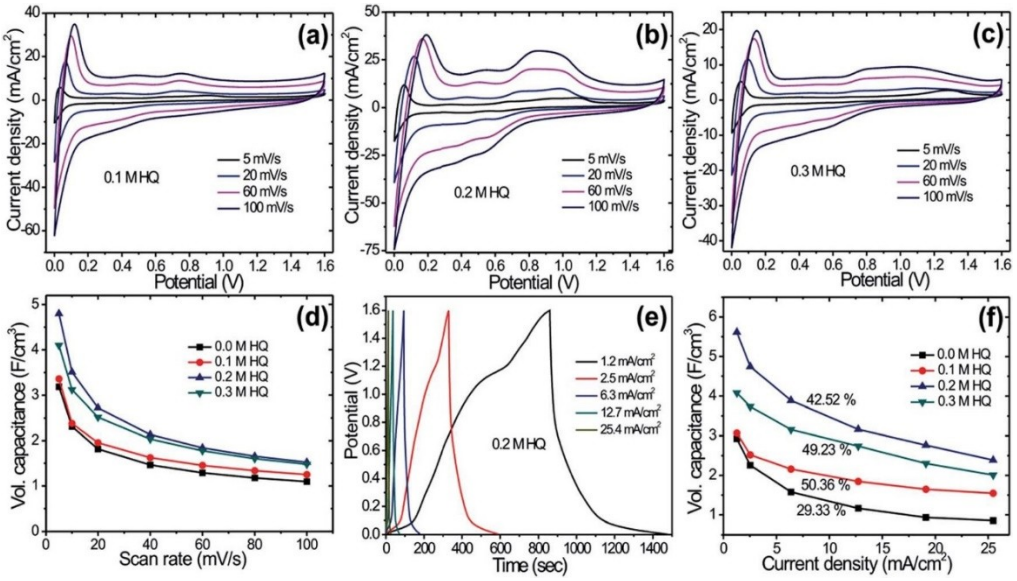

Fig. 7 (a–c) CV curves of rGO–PMo_{12} symmetric cells with HQ doped gel-electrolyte of different concentrations at various scan rates, (d) summary of volumetric capacitance vs. scan rate of rGO–PMo_{12} cell for different HQ concentrations, (e) CD curves of the rGO–PMo_{12} symmetric cell with the 0.2 M HQ doped electrolyte at different current densities, and (f) variation of volumetric capacitances with the current density of the rGO–PMo_{12} cell for different concentrations of HQ.

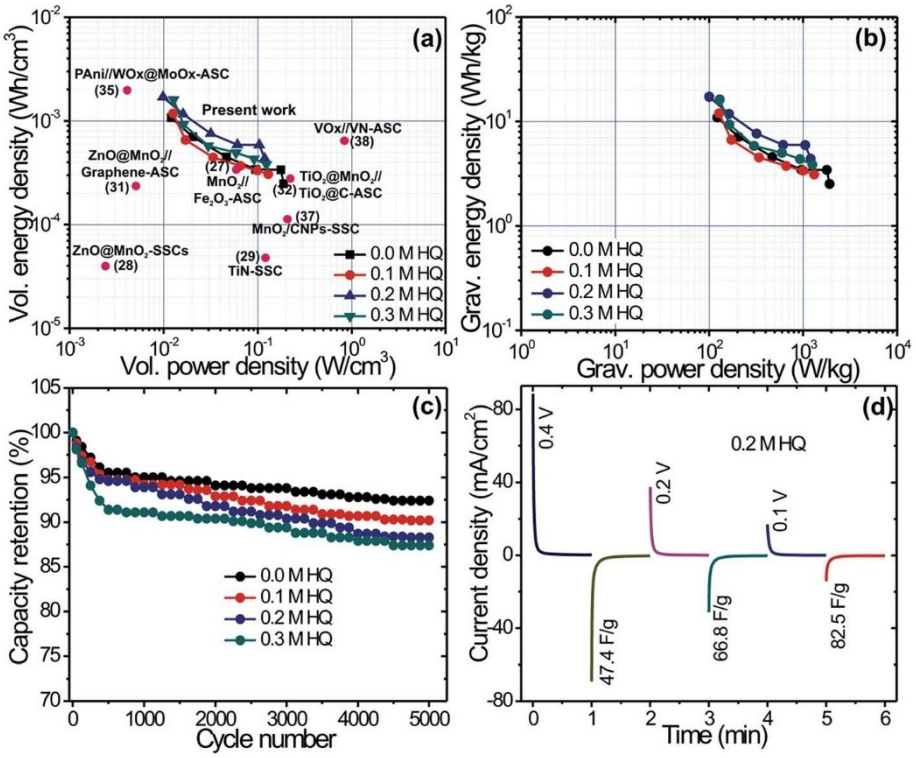

Fig. 8 (a and b) Volumetric and gravimetric energy/power densities of the rGO–PMo_{12} symmetric cell with different concentrations of HQ doped electrolytes in Ragone plots, respectively, (c) capacity retention of the rGO–PMo_{12} symmetric cell measured by a cycling charge– discharge test at a current density of 12.7 mA cm^{-2} in a redox-active electrolyte, and (d) chronoamperometry charge/discharge curves measured at different cell potentials 0.4, 0.2 and 0.1 V for 1 min, after a 20 min conditioning period (full discharge to 0 V).

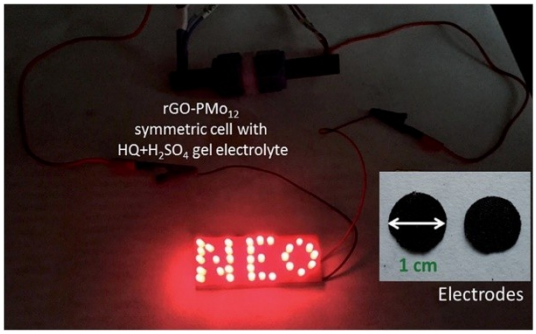

Fig. 9 Thirty-one (31) LED indicators with the word "NEO" powered by the rGO–PMo_{12} symmetric cell with the 0.2 M HQ doped polymer gel- electrolyte